EDGE ARTICLE

Graphene nucleation on a surface-molten copper catalyst: quantum chemical molecular dynamics simulations†

Hai-Bei Li,[ab] Alister J. Page,*[c] Christian Hettich,[d] Bálint Aradi,[d] Christof Köhler,[d] Thomas Frauenheim,[d] Stephan Irle*[e] and Keiji Morokuma*[b]

Chemical vapor deposition (CVD) growth of graphene on Cu(111) has been modeled with quantum chemical molecular dynamics (QM/MD) simulations. These simulations demonstrate at the atomic level how graphene forms on copper surfaces. In contrast to other popular catalysts, such as nickel and iron, copper is in a surface molten state throughout graphene growth at CVD-relevant temperatures, and graphene growth takes place without subsurface diffusion of carbon. Surface Cu atoms have remarkably high mobilities on the Cu(111) surface, both before and after graphene nucleation. This surface mobility drives "defect healing" processes in the nucleating graphene structure that convert defects such as pentagons and heptagons into carbon hexagons. Consequently, the graphene defects that become "kinetically trapped" using other catalysts, such as Ni and Fe, are less commonly observed in the case of Cu. We propose this mechanism to be the basis of copper's ability to form high-quality, large-domain graphene flakes.

1. Introduction

Graphene is a two-dimensional carbon material consisting of a single layer of sp²-hybridized carbon atoms arranged in a hexagonal lattice. It has attracted considerable attention over the past decade due to its remarkable electronic, optical, and mechanical properties,[1–3] which make it one of the most promising candidates for next-generation electronic applications. However, development of graphene-based devices requires the commercial-scale synthesis of large-area, high-quality graphene, and this remains a significant challenge. One of the most promising and versatile growth methods is chemical vapor deposition (CVD) of carbonaceous gases on transition metal substrates such as Ni,[4–6] Ru,[7,8] Ir,[9,10] Cu[11–14] and most recently Ag.[15] CVD has thus far been the preferred method of

producing graphene, due to its ability to produce high-quality graphene films with large domains.[16,17] Of particular importance in this respect are Ni[6,18–20] and more recently Cu catalysts,[12,14,21–26] which are most widely used for graphene formation.

One limitation of Ni catalysts for CVD graphene growth is their propensity to form multi-layered graphene sheets,[27] as opposed to single-layer graphene, and this presumably arises from a metastable Ni-carbide phase at CVD-relevant temperatures. Ni exhibits both high carbon solubility and bulk carbon diffusivity, and on this basis Weatherup *et al.*[28] have proposed that graphene growth is neither purely a bulk precipitation process nor a catalytic surface process, and that graphene growth on Ni(111) consists of four main steps: (1) adsorption and catalytic decomposition of hydrocarbon precursors; (2) diffusion and dissolution of carbon atoms into the Ni subsurface; (3) precipitation of dissolved carbon atoms onto the metal surface; (4) surface nucleation and growth of graphene. We have investigated the last two steps in our previous work,[29–32] which highlighted the role played by subsurface carbon on graphene formation. Indeed, subsurface carbon density can single-handedly determine the type of carbon structure formed on the catalyst surface.[29] Precipitation of subsurface carbon onto the Ni(111) surface induces significant structural disorder in the Ni surface. The quality of graphene grown on a disordered Ni surface is also higher than that on intact and immobile surfaces,[32] and this points to the possibility that the surface morphology and mobility of catalyst atoms are important factors in the quality of graphene flakes.

[a]School of Ocean, Shandong University, Weihai 264209, China

[b]Fukui Institute for Fundamental Chemistry, Kyoto University, 34-4 Nishihiraki-cho, Sakyo-ku, Kyoto, 606-8103, Japan. E-mail: morokuma@fukui.kyoto-u.ac.jp; Tel: +81 75 711-7843

[c]Newcastle Institute for Energy and Resources, The University of Newcastle, Callaghan 2308, Australia. E-mail: alister.page@newcastle.edu.au; Tel: +61-24033-9357

[d]Bremen Center for Computational Materials Science, University of Bremen, Am Fallturm 1, D-28359, Bremen, Germany

[e]WPI-Institute of Transformative Bio-Molecules (ITbM) & Department of Chemistry, Graduate School of Science, Nagoya University, Furu-cho, Chikusa-ku, Nagoya 464-8602, Japan. E-mail: sirle@chem.nagoya-u.ac.jp; Tel: +81 52 747-6397

† Electronic supplementary information (ESI) available: The snapshots at 50 ps and carbon ring population for 10 trajectories; QuickTime movie depicting the defect healing process in trajectory 6. See DOI: 10.1039/c4sc00491d

Cu, as opposed to Ni, predominantly forms single-layer graphene exclusively *via* surface catalytic reactions and processes,[17] and this can be explained by its ultralow carbon solubility.[33] This, combined with the lower market price of copper, have made it perhaps the most widely preferred catalyst for CVD graphene production. Numerous efforts have been made to produce large-scale monolayer graphene on Cu catalysts.[16,17] Several groups have focused on optimizing the parameters of CVD growth, including controlling the growth pressure and temperature to grow uniform large-area graphene (ref. 17 and therein). Wood *et al.*[22] proposed that growth of high-quality, large domain graphene depends on the underlying Cu crystal structure, and for this reason the Cu(111) surface is preferable for high-quality/large-domain monolayer graphene. However, large-size, spatially self-aligned, and single-crystalline hexagonal graphene flakes have been produced on *liquid* Cu surfaces, implicating pronounced surface atom mobility in the formation of high-quality graphene.[14]

The role of surface morphology on graphene formation with Cu catalysts therefore remains an important issue. This is particularly true with respect to the earliest stages of graphene growth, *i.e.* "nucleation", however probing this experimentally is a great challenge. Despite a number of computational investigations of graphene nucleation on Cu,[34–36] none have addressed this issue in detail. Current pictures of graphene nucleation proposed thus far rest generally upon the assumption that the step-edge defect, and more generally, the catalyst surface, remains an ideal, smooth, and static structure throughout the nucleation process. It is noted that there is no experimental evidence to support this assumption, and recent simulations concerning Ni catalysts indicate that the opposite is in fact the case.[29,31] The dynamics of the Cu surface during graphene nucleation have been investigated over limited time-scales.[37] This has shown that carbon–metal bridging structures, which are induced by carbon adatoms on the catalyst surface, strongly influence the dynamics of graphene nucleation. This is also the case on Ni and Fe catalysts.[30] In the case of Cu, it is therefore plausible that the role of the catalyst surface during graphene growth, while still poorly understood, is perhaps less passive than originally thought.

In this work, we present quantum chemical simulations towards this end. We provide the first comprehensive atomistic picture of nucleation and growth of graphene on the Cu(111) surface. We demonstrate here that the physical state of the Cu surface region plays a key role in graphene growth. In particular, we reveal a potential mechanism that explains copper's intrinsic ability to form higher quality graphene structures compared with Ni and Fe catalysts, and attribute this phenomenon to the healing role played by highly mobile Cu surface atoms.

2. Computational details

We have investigated graphene nucleation on transition metal catalyst (111) surfaces on a number of previous occasions using QM/MD simulations,[29–32] and in this work we employ a similar approach. Our QM/MD approach involves the integration of the classical equations of motion, in conjunction with a QM

potential. The latter in this case is the 2nd order (self-consistent charge) density functional tight-binding (SCC-DFTB, also sometimes called DFTB2) method, as implemented in the DFTB+ program.[38] A finite electronic temperature[39] of 3000 K was enforced throughout all simulations, and so orbital occupations for molecular orbitals near the Fermi level were described by a Fermi–Dirac distribution function. In practical terms, this alleviates DFTB convergence issues that arise from the presence of many near-degenerate Cu d orbitals and unterminated carbon "dangling" bonds, and has been used and validated by us extensively in previous investigations of carbon nanostructure growth.[40,41] The nuclear equations of motion were integrated using the Velocity Verlet algorithm,[42] with the NVT ensemble being maintained *via* a Nosé–Hoover chain thermostat (chain-length 3)[43] connected to the degrees of freedom of the system. The nuclear temperature was maintained at 1180 K throughout all simulations. The Cu–Cu/Cu–C DFTB electronic parameters employed here are those developed by Cui *et al.*,[44] and are verified for systems typical of graphene growth in the ESI.† The Cu–Cu repulsive DFTB potential was developed in this work using the automatic parameterization scheme of Bodrog *et al.*[45] based on the energies of fcc bulk Cu using density functional theory (DFT) calculations. Full details and benchmark data for the Cu–Cu repulsive potential is provided in the ESI.† The C–C DFTB parameters are those from the mio-0-1 DFTB parameter set, included in the trans3d-0-1 parameter set[46] that was used in our previous work.

For the QM/MD simulations, a four-layer Cu(111) model surface consisting of a 6×6 slab (144 atoms in total) was employed. The bottom layer in this model surface was frozen throughout all simulations, as an approximation to the underlying bulk region. Three-dimensional periodic boundary conditions (PBC) were enforced on this model system for all simulations. Our treatment of PBC employed the Γ-point approximation. Adjacent Cu(111) surfaces were separated by a vacuum region of 10 nm. Ten replicas of this model structure were then thermally equilibrated for 10 ps at 1180 K with random initial velocities to generate 10 independent initial structures for the subsequent graphene growth trajectories. The latter began by adsorbing 30 C_2 moieties randomly onto the equilibrated Cu(111) surfaces with randomly selected orientations. Each C_2 species was placed *ca.* 0.25 nm above the surface. The initial velocities of these carbon atoms were defined randomly according to a Maxwell–Boltzmann distribution at 1180 K. Graphene growth was then simulated at 1180 K for a period of 50 ps. This methodology closely follows the approach we took for simulating Haeckelite and graphene growth on Ni(111).[32]

Atomic binding energies of metal surfaces were calculated using plane-wave DFT, as implemented in the Vienna *ab initio* simulation package (VASP).[47] The PBE exchange-correlation functional[48] was employed throughout. A four-layer slab with 4×4 atoms in each layer was used to model the bcc Cu(111) surface, with each slab separated by 5 nm. In these DFT calculations, a k-point sampling of $2 \times 2 \times 1$ and a plane wave cutoff of 400 eV were employed to ensure adequate convergence.

To analyze the physical state of the Cu(111) surface before and after graphene growth, we employed the Lindemann index, δ,[49]

$$\delta = \frac{1}{N(N-1)} \sum_{i<j} \frac{\sqrt{\langle r_{ij}^2 \rangle_T - \langle r_{ij} \rangle_T^2}}{\langle r_{ij} \rangle_T} \quad (1)$$

Here N is the number of atoms, r_{ij} is the instantaneous distance between atoms i and j, and the brackets denote thermal averaging over a finite interval of time at temperature T. While we know of no application of the Lindemann index in the context of graphene nucleation and growth, it has been shown on a number of occasions to be an accurate probe of the catalyst phase during carbon nanotube nucleation and growth.[50–52]

3. Results and discussion

3.1. Phase of the Cu(111) surface during graphene growth

Simulations of the pristine Cu(111) surface are compared with a pristine Ni(111) surface in Fig. 1.

Quite remarkably, the crystalline structure of the Cu(111) surface obtained from a 0 K geometry relaxation is lost almost immediately in the MD simulation at 1180 K. The extent of disorder in this structure is significant, with atoms in the surface layer diffusing into subsurface layers, and *vice versa*. Interestingly, the temperature of this simulation is below the bulk melting point of Cu (1385 K). We note that the binding energy of individual copper atoms in the Cu(111) surface predicted with SCC-DFTB is *ca.* 1.5 eV lower than that predicted

with PBE (see ESI, Fig. S5†). This may suggest that higher copper atom mobility is an artifact of the weaker binding predicted with SCC-DFTB. However, the same difference between PBE and SCC-DFTB is observed for Ni(111). Similarly, the PBE binding energy for Cu(111) is *ca.* 0.8 eV lower than that for Ni(111). The observed mobility of the atoms in the Cu(111) surface therefore cannot be attributed solely to SCC-DFTB's underestimation of the Cu–Cu interaction. In any case, natural fluctuations in temperature throughout the simulation, induced by the thermostat algorithm itself, are likely to outweigh this influence. Furthermore, both of these factors are overshadowed by highly fluctuating local temperatures in the simulation, which result from the repeated exothermic C–C bond formation that defines graphene formation. Cu(111) therefore exists as a "surface-molten" species under these conditions (in line with recent experimental reports of Cu(111)-catalyzed graphene growth[53]), and features surface atoms with remarkably high mobilities. The surface-molten phenomenon results from the pre-melting of the surface region below the bulk melting point, and has been observed for many metals previously.[54,55] In contrast, at the same temperature the Ni(111) surface remains effectively unchanged from its 0 K crystalline form (Fig. 1(b)). Compared with the high mobility of Cu atoms, the surface Ni atoms remain tightly bound within the crystal lattice structure. Ni atoms in the Ni(111) surface are far more "passive" compared to their Cu counterparts, and the resultant increase in stability is consistent with the higher melting temperature of bulk Ni, 1728 K (*ca.* 548 K above the current temperature). Furthermore, the difference between surface mobility of Cu and Ni atoms can be described with recourse to the evolution of the phase of the metal surface, estimated by monitoring δ during the annealing process (Fig. 1(c)). It is immediately apparent from this figure that the Ni surface at 1180 K is in the solid phase (the commonly accepted value for the Lindemann index that signifies the solid/liquid phase transition is $\delta = 0.1$ (ref. 56)). The small variation of δ in the range of 1–10 ps implies the limited mobility of Ni atoms in the surface. In contrast, the Cu surface exhibited wide variations in δ with respect to simulation time, implying rapid disordering of the Cu surface.
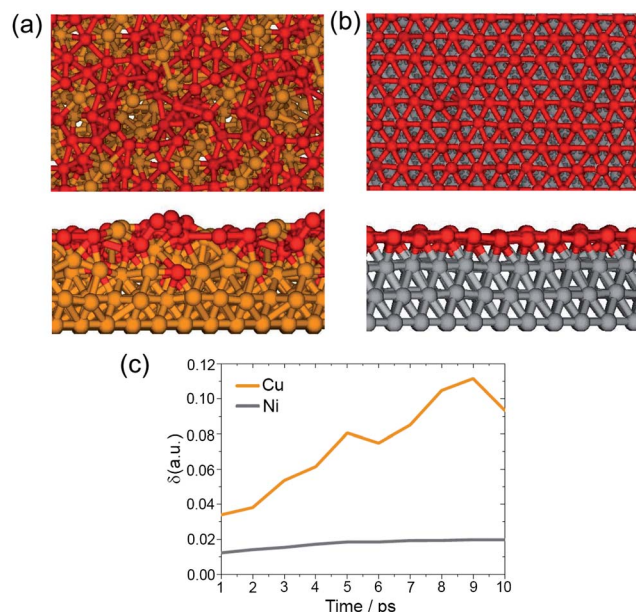
3.2. Graphene nucleation and defect healing on Cu(111)

We turn now to a discussion of the graphene nucleation mechanism on Cu(111). We have studied graphene nucleation on Ni(111) and Fe(111) surfaces on a number of previous occasions.[29–32] These simulations have shown that graphene quality is influenced by the presence of a hexagonal template or "nucleation seed" on the catalyst surface, the origin of carbon feedstock and both the surface and subsurface carbon density. In the presence of a high surface carbon density on pristine Ni(111),[32] nucleation consisted of a swift transition of long polyyne chains into a connected sp²-carbon network. In the absence of a hexagonal template, a structure akin to penta-heptite, also called Haeckelite,[57,58] was formed preferentially. The simulations in the present work for Cu employ an identical carbon density to that employed by us previously for Ni, and so it is reasonable to predict that nucleation should proceed along

Fig. 1 Snapshots of (a) Cu(111) and (b) Ni(111) model surface at 10 ps; (c) δ for Cu(111) and Ni(111) for the first 10 ps annealing process. While Ni(111) remains in an essentially crystalline state, Cu(111) immediately transforms into a surface-molten state at 1180 K. For fully equilibrated Cu(111) and Ni(111), δ is 0.28 and 0.02, respectively. Red atoms denote those originally in the surface layer.

a comparable path, resulting in the formation of a highly defective structure akin to Haeckelite. However, somewhat surprisingly, this is not the case.

Snapshots depicted in Fig. 2(a) typify the dynamics of graphene nucleation observed on the surface-molten Cu(111) surface. As predicted, the basic chemical reaction observed here is similar to that observed on Ni(111). The formation of extended polyyne chains and Y-junction precursors were common and immediate following the deposition of a high density of C_2 fragments. As we have previously noted in the context of fullerene, carbon nanotube and graphene formation, these structural precursors are seemingly a cornerstone of carbon nanostructure growth.[51,59] In Fig. 2(a), the snapshot at 0.7 ps shows that nearly all original C_2 fragments have connected to each other irregularly, and cover the disordered Cu surface almost completely. Complete coverage is not anticipated, since the carbon density present here is approximately 83% of that required to form monolayer graphene. Fig. 2(a) shows that pentagon/hexagon rings and extended polyyne chains (>10 carbon atoms) coexist at 0.7 ps. Comparing the Cu(111) structures at 0.0 ps and 0.7 ps, it is immediately apparent that the presence of carbon on the Cu surface strongly affects the latter's morphology, *increasing* its structural disorder.

Following the formation of these polyyne chains, subsequent ring condensation and the formation of sp²-hybridized islands is rapid. Due to the somewhat artificial nature of the starting point of this simulation, the kinetics of graphene formation observed here is irrelevant in the absolute sense (relative

kinetics can and will be compared below). However, as shown below in detail, this simulation provides the first evidence of defect healing during graphene growth, which potentially underpins the high structural quality observed in graphene grown on Cu catalysts.[14,25] It is already established that defect healing processes play a predominant role in chirality control during carbon nanotube growth.[60]

Fig. 2(a) shows a structure (1.4 ps) consisting of approximately 50% structural defects, *i.e.* pentagonal and heptagonal rings. Following a further 50 ps, this highly defective structure – reminiscent of Haeckelite – was transformed into an essentially pristine graphene structure, *i.e.* one composed almost completely of carbon hexagons. This is confirmed in Fig. 2(b), which quantifies the population of different polygonal carbon rings in the structure during the course of the trajectory. The transformation of this originally defective structure took place *via* a number of chemical pathways, yet in all cases was driven by the mobility of the Cu atoms in the underlying catalyst surface. For example, the pentagon–heptagon defect (indicated by the circle in Fig. 2(a)) observed at 1.4 ps was healed by 2.67 ps. This process, shown in ESI Movie S1,† is driven by the diffusion of a single Cu atom in the surface layer which opens a vacancy in the Cu(111) surface, and consequently forces the cleavage of a C–C bond in the heptagon. The terminal carbon in the polyyne chain thus formed then resides in the surface vacancy, due to attractive forces between it and the Cu surface, and this facilitates the formation of the hexagon in place of the original heptagon defect. The attraction between this terminal carbon atom and the Cu surface is sufficiently strong that it is
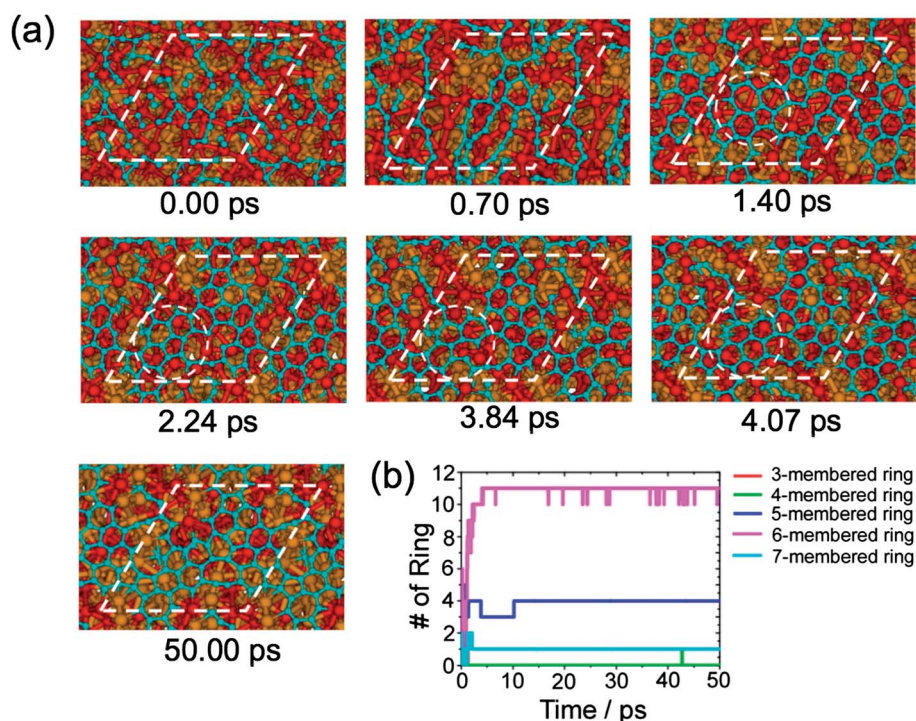

Fig. 2 (a) Evolution of trajectory 6, depicting graphene nucleation and defect ring healing on Cu(111). Defect healing mechanisms discussed in the text (white circle) are included in the ESI (see Movie S1†). (b) Formation statistics of polygonal carbon rings as a function of simulation time for trajectory 6.

cleaved from the hexagon and diffuses into the subsurface region of the catalyst. The neighboring pentagon defect was subsequently healed into a hexagon *via* a comparable chemical route – first C–C bond cleavage and then ring closure, both being driven by the dynamics of the underlying substrate. The fact that the heptagon was healed prior to the pentagon being converted is consistent with the relative kinetic stabilities of carbon pentagon and heptagon rings, the former being considerably less flexible than the latter.

Although it may be expected that copper's ability to aggressively heal defects in the graphene structure should correlate with a relatively high Cu–C bond strength, this is in fact not the case. End-on σ-bonding between C and Cu is actually weaker than that for both Fe and Ni (2.13 eV, *vs.* 2.94 and 2.76 eV respectively). Similarly, side-on π-bonding between C and Cu is weaker than that for Fe (0.0 eV *vs.* 0.27 eV), while being equal to that for Ni.[30] In other words, defect healing cannot be explained in this case simply with recourse to thermodynamics. Instead, we propose here that the catalyst phase is a key factor that determines a catalyst's ability to heal graphitic carbon defects, both in graphene and carbon nanotubes. In particular, since liquid phase catalysts exhibit higher surface mobilities than solid phase catalysts, they are *kinetically* more equipped to disrupt the adsorbed sp^2 carbon network, thereby aiding its reconfiguration to a more thermodynamically stable one.
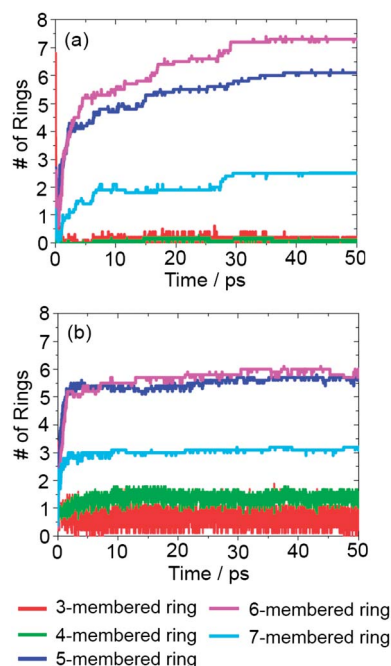

Fig. 3 Average polygonal carbon ring populations observed during graphene nucleation on (a) Cu(111) and (b) Ni(111)[32] surfaces. The final graphene structures observed on Cu(111) take an order of magnitude longer to be achieved compared with those on Ni(111), as the atomic configuration of the structure is constantly rearranged by defect healing mechanisms. By contrast, the final graphene structure on Ni(111) is obtained almost immediately, within *ca.* 5 ps. All data averaged over 10 trajectories.

3.3. Comparison of graphene growth on Ni and Cu catalysts

This argument is corroborated further by Fig. 3, which compares polygonal carbon ring formation data observed during graphene nucleation on Cu(111) and Ni(111) (see also Fig. S2 in the ESI†). The formation of polygonal carbon rings on the molten Cu(111) is remarkably different compared to that observed on Ni(111). Ring formation in the latter case is essentially instantaneous (due to the artificial nature of the initial conditions employed), with the final structure obtained essentially within *ca.* 2.5 ps. Conversely, using Cu(111), the ring formation statistics evolve over a much longer period. Initially increasing sharply (*ca.* 5 ps), it takes a further 30 ps for the ultimate populations of pentagons, hexagons and heptagons to be obtained on Cu(111). This is because the nucleating graphene structure is constantly being reorganized by the underlying catalyst atoms towards the most thermodynamically favorable configuration (one consisting entirely of hexagons). Consequently, the population of hexagons observed in graphene becomes maximized compared to heptagons and, more importantly, pentagons. This is not the case on Ni(111), for which approximately equal populations of pentagons and hexagons are formed.

The defining characteristic of copper catalysts, at least in the context of graphene formation, is the mobility of Cu atoms in the surface and subsurface regions. This mobility is the root cause of copper's ability to actively heal structural defects in the adsorbed graphene film, presumably during and after graphene growth. Notably, the mobility of surface Cu atoms does not decrease following the formation of the overlying graphene structure, as indicated by δ, shown in Fig. 4. This is not the case in Ni(111),[32] as mentioned previously, which remains in the solid phase throughout the nucleation process. Under conditions of high surface carbon density, such as those employed here, a pre-existing hexagonal template is required in order to induce further hexagon formation on Ni(111), otherwise pentagon and heptagon defects dominate the carbon structure. Furthermore, defect healing processes such as those observed here are seldom, if ever, observed under equivalent conditions using a Ni(111) catalyst. This is consistent with the more pronounced crystallinity in Ni(111) at 1180 K, evident in Fig. 1(b). Previous investigations have shown graphene growth on Ni(111) drives the self-assembly of step-edge defects on the catalyst surface – subsurface carbon present during graphene growth on a pristine Ni(111) terrace induces the formation of step-edge defects in the Ni(111) structure.[29,31] However, due to the low carbon solubility of Cu, a well-defined step edge in the case of Cu(111) is not observed, as shown in Fig. 2. This can be explained in terms of the relative mobilities of Ni/Cu surface atoms. The latter are so diffusive that the growing graphene structure is incapable of holding them in place, which would be necessary for step-edge formation. The consequence of this is that defects at the edge of the growing graphene sheet on Ni(111) are kinetically "trapped", and potentially remain in the structure for longer time scales, and potentially indefinitely. On the other hand, on Cu(111) they are removed *during growth via* various chemical pathways, as discussed above.
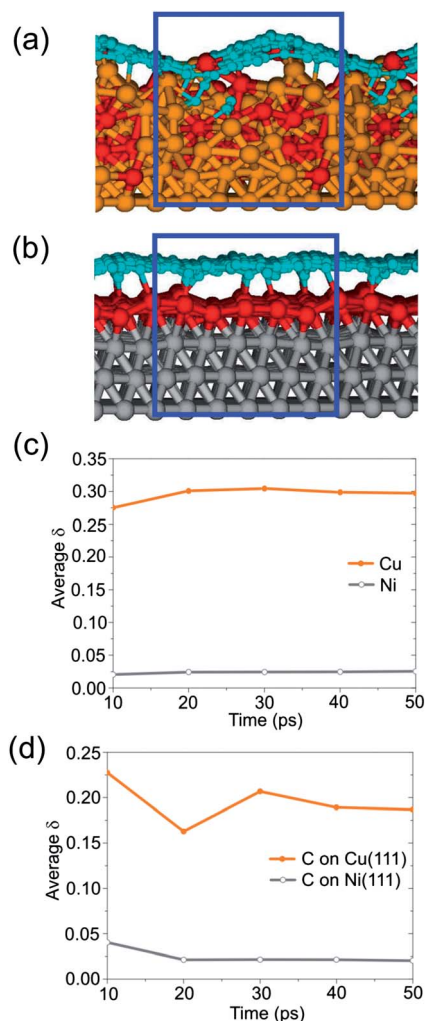
Fig. 4 (a) Cu(111) and (b) Ni(111) surfaces after 50 ps QM/MD simulation of trajectory 6, viewed side-on. The blue box denotes the PBC supercell. δ for (c) Cu(111) and Ni(111) surfaces and (d) carbon atoms on Cu(111)/Ni(111) during the simulation at an interval of 10 ps averaged over 10 trajectories. For graphene nucleation on Cu(111), both the catalyst and the nucleating carbon structure exhibit significantly higher mobilities than those observed during graphene nucleation on Ni(111). This is due to the prevalence of defect healing processes in the former case, which increases carbon atom mobility on the Cu(111) surface.

Atomic binding energies for the Cu(111) and Ni(111) surfaces (defined as $E_{M(111)} - E_M - E_{M(111)-M}$, where $E_{M(111)}$ is the energy of the complete surface, E_M that of an isolated atom, and $E_{M(111)-M}$ that of the surface with an atom removed) computed using DFT are consistent with observations made during QM/MD simulations. The atomic binding energy for Cu(111) is 4.52 eV, and this is significantly lower than that for Ni(111) (6.32 eV). Thus, the Cu–Cu bond is inherently weaker than the Ni–Ni bond; this is not surprising considering the relative bulk melting points. These relative bond strengths are also consistent with Fig. 4(a) and (b) which show a remarkable difference in the structure of the catalysts following graphene formation. Fig. 4(a) further highlights the defect-healing role of the surface Cu atoms, through the presence of "point defects" –

Cu atoms that have been incorporated into the growing graphene flake and no longer formally reside in the catalyst structure itself. In contrast, Fig. 4(b) *reinforces* the crystallinity observed within the Ni(111) surface at 1180 K. The prevalence of defect healing in the case of Cu(111) also manifests in the Lindemann indices of the nucleating carbon structure, shown in Fig. 4(d). δ for Cu(111) is far higher than that observed for Ni(111), indicating that the surface-adsorbed carbon structure on Cu(111) exhibits far greater conformational freedom than that on Ni(111).

4. Conclusion

We have presented quantum chemical simulations of graphene nucleation on Cu(111) at 1180 K, revealing a detailed picture of the growth mechanism of graphene on Cu. These simulations highlight the key role the physical state of the catalyst plays both on graphene growth and mechanisms of defect healing during graphene growth. Throughout the nucleation process, Cu(111) remains in a surface-molten state, one in which surface Cu atoms have remarkably high mobilities. The rapid diffusion of surface Cu atoms drives defect-healing mechanisms within the graphene structure during growth, and is consistent with the recent observation by the Ruoff group that millimeter-size single-crystal graphene can be grown by suppressing the evaporative loss of Cu during low pressure CVD.[53] This phenomenon has so far not been observed on other transition metal catalysts, such as Ni and Fe, at least on these timescales. Thus, it is possible that graphene defects such as pentagons and heptagons on Ni and Fe catalysts, once formed, remain "trapped" in the structure as it extends further over the catalyst surface. Conversely, we show here that defects at the edge of the growing graphene flake on Cu are almost immediately removed, through the influence of the underlying, highly diffusive copper atoms. We propose this as a mechanism to explain the high structural quality of graphene grown on Cu observed in CVD experiments. Importantly, copper's ability to heal defective graphitic structures observed here does not correlate with a purely thermodynamic picture of defect healing. The interaction between Cu and C is weaker than that between C and both Fe and Ni. Thus, thermodynamics alone does not drive defect healing – it is a phenomenon driven intrinsically by kinetic factors. On this basis, it is evident that the phase of the catalyst is a key factor determining the ability of a catalyst to heal defective graphitic structures.

Acknowledgements

supercomputer time at the Institute for Molecular Science (IMS) in Okazaki, Japan.

References

1 A. A. Balandin, S. Ghosh, W. Bao, I. Calizo, D. Teweldebrhan, F. Miao and C. N. Lau, *Nano Lett.*, 2008, **8**, 902–907.

2 A. H. Castro Neto, F. Guinea, N. M. R. Peres, K. S. Novoselov and A. K. Geim, *Rev. Mod. Phys.*, 2009, **81**, 136–162.

3 P. Avouris, *Nano Lett.*, 2010, **10**, 4285–4294.

4 X. Li, W. Cai, L. Colombo and R. S. Ruoff, *Nano Lett.*, 2009, **9**, 4268–4272.

5 A. J. Pollard, R. R. Nair, S. N. Sabki, C. R. Staddon, L. M. A. Perdigao, C. H. Hsu, J. M. Garfitt, S. Gangopadhyay, H. F. Gleeson, A. K. Geim and P. H. Beton, *J. Phys. Chem. C*, 2009, **113**, 16565–16567.

6 J. Lahiri, T. Miller, K. Adamska, I. I. Oleynik and M. Batzill, *Nano Lett.*, 2011, **11**, 518–522.

7 E. Sutter, P. Albrecht and P. Sutter, *Appl. Phys. Lett.*, 2009, **95**, 133109.

8 Y. Cui, Q. Fu, H. Zhang and X. Bao, *Chem. Commun.*, 2011, **47**, 1470–1472.

9 J. Coraux, A. T. N'Diaye, M. Engler, C. Busse, D. Wall, N. Buckanie, F.-J. Meyer zu Heringdorf, R. van Gastel, B. Poelsema and T. Michely, *New J. Phys.*, 2009, **11**, 023006.

10 P. Lacovig, M. Pozzo, D. Alfe, A. Baraldi and S. Lizzit, *Phys. Rev. Lett.*, 2009, **103**, 166101.

11 L. Gao, J. R. Guest and N. P. Guisinger, *Nano Lett.*, 2010, **10**, 3512–3516.

12 S. Nie, J. M. Wofford, N. C. Bartelt, O. D. Dubon and K. F. McCarty, *Phys. Rev. B: Condens. Matter Mater. Phys.*, 2011, **84**, 155425.

13 R. G. Van Wesep, H. Chen, W. Zhu and Z. Zhang, *J. Chem. Phys.*, 2011, **134**, 171105–171104.

14 D. Geng, B. Wu, Y. Guo, L. Huang, Y. Xue, J. Chen, G. Yu, L. Jiang, W. Hu and Y. Liu, *Proc. Natl. Acad. Sci. U. S. A.*, 2012, **109**, 7992–7996.

15 B. Kiraly, E. V. Iski, A. J. Mannix, B. L. Fisher, M. C. Hersam and N. P. Guisinger, *Nat. Commun.*, 2013, **4**, 2804.

16 K. Yan, L. Fu, H. Peng and Z. Liu, *Acc. Chem. Res.*, 2013, **46**, 2263–2274.

17 Y. Zhang, L. Zhang and C. Zhou, *Acc. Chem. Res.*, 2013, **46**, 2329–2339.

18 S. J. Chae, F. Güneş, K. K. Kim, E. S. Kim, G. H. Han, S. M. Kim, H.-J. Shin, S.-M. Yoon, J.-Y. Choi, M. H. Park, C. W. Yang, D. Pribat and Y. H. Lee, *Adv. Mater.*, 2009, **21**, 2328–2333.

19 W. Zhao, S. M. Kozlov, O. Höfert, K. Gotterbarm, M. P. A. Lorenz, F. Viñes, C. Papp, A. Görling and H.-P. Steinrück, *J. Phys. Chem. Lett.*, 2011, **2**, 759–764.

20 R. Addou, A. Dahal, P. Sutter and M. Batzill, *Appl. Phys. Lett.*, 2012, **100**, 021601–021603.

21 G. H. Han, F. Güneş, J. J. Bae, E. S. Kim, S. J. Chae, H.-J. Shin, J.-Y. Choi, D. Pribat and Y. H. Lee, *Nano Lett.*, 2011, **11**, 4144–4148.

22 J. D. Wood, S. W. Schmucker, A. S. Lyons, E. Pop and J. W. Lyding, *Nano Lett.*, 2011, **11**, 4547–4554.

23 B. Hu, H. Ago, Y. Ito, K. Kawahara, M. Tsuji, E. Magome, K. Sumitani, N. Mizuta, K.-I. Ikeda and S. Mizuno, *Carbon*, 2012, **50**, 57–65.

24 A. Kumar, A. A. Voevodin, D. Zemlyanov, D. N. Zakharov and T. S. Fisher, *Carbon*, 2012, **50**, 1546–1553.

25 Y. A. Wu, Y. Fan, S. Speller, G. L. Creeth, J. T. Sadowski, K. He, A. W. Robertson, C. S. Allen and J. H. Warner, *ACS Nano*, 2012, **6**, 5010–5017.

26 Y. Wu, Y. Hao, H. Y. Jeong, Z. Lee, S. Chen, W. Jiang, Q. Wu, R. D. Piner, J. Kang and R. S. Ruoff, *Adv. Mater.*, 2013, **25**, 6744–6751.

27 A. Reina, X. Jia, J. Ho, D. Nezich, H. Son, V. Bulovic, M. S. Dresselhaus and J. Kong, *Nano Lett.*, 2008, **9**, 30–35.

28 R. S. Weatherup, B. C. Bayer, R. Blume, C. Ducati, C. Baehtz, R. Schlögl and S. Hofmann, *Nano Lett.*, 2011, **11**, 4154–4160.

29 Y. Wang, A. J. Page, H.-B. Li, H.-J. Qian, M.-g. Jiao, Z.-J. Wu, K. Morokuma and S. Irle, *Nanoscale*, 2014, **6**, 140–144.

30 A. J. Page, Y. Wang, H.-B. Li, S. Irle and K. Morokuma, *J. Phys. Chem. C*, 2013, **117**, 14858–14864.

31 H.-B. Li, A. J. Page, Y. Wang, S. Irle and K. Morokuma, *Chem. Commun.*, 2012, **48**, 7937–7939.

32 Y. Wang, A. J. Page, Y. Nishimoto, H.-J. Qian, K. Morokuma and S. Irle, *J. Am. Chem. Soc.*, 2011, **133**, 18837–18842.

33 C. Mattevi, H. Kim and M. Chhowalla, *J. Mater. Chem.*, 2011, **21**, 3324–3334.

34 H. Chen, W. Zhu and Z. Zhang, *Phys. Rev. Lett.*, 2010, **104**, 186101.

35 J. Gao, J. Yip, J. Zhao, B. I. Yakobson and F. Ding, *J. Am. Chem. Soc.*, 2011, **133**, 5009–5015.

36 J. Gao, J. Zhao and F. Ding, *J. Am. Chem. Soc.*, 2012, **134**, 6204–6209.

37 P. Wu, W. Zhang, Z. Li, J. Yang and J. G. Hou, *J. Chem. Phys.*, 2010, **133**, 071101–071104.

38 B. Aradi, B. Hourahine and T. Frauenheim, *J. Phys. Chem. A*, 2007, **111**, 5678–5684.

39 M. Weinert and J. W. Davenport, *Phys. Rev. B*, 1992, **45**, 13709–13712.

40 A. J. Page, Y. Ohta, S. Irle and K. Morokuma, *Acc. Chem. Res.*, 2010, **43**, 1375–1385.

41 S. Irle, G. Zheng, Z. Wang and K. Morokuma, *J. Phys. Chem. B*, 2006, **110**, 14531–14545.

42 W. C. Swope, H. C. Andersen, P. H. Berens and K. R. Wilson, *J. Chem. Phys.*, 1982, **76**, 637–649.

43 G. J. Martyna, M. L. Klein and M. Tuckerman, *J. Chem. Phys.*, 1992, **97**, 2635–2643.

44 Q. Cui, private communication.

45 Z. N. Bodrog, B. L. Aradi and T. Frauenheim, *J. Chem. Theory Comput.*, 2011, 7, 2654–2664.

46 G. Zheng, H. A. Witek, P. Bobadova-Parvanova, S. Irle, D. G. Musaev, R. Prabhakar, K. Morokuma, M. Lundberg, M. Elstner, C. Kohler and T. Frauenheim, *J. Chem. Theory Comput.*, 2007, **3**, 1349.

47 G. Kresse and J. Furthmüller, *Phys. Rev. B*, 1996, **54**, 11169–11186.

48 J. P. Perdew, J. A. Chevary, S. H. Vosko, K. A. Jackson, M. R. Pederson, D. J. Singh and C. Fiolhais, *Phys. Rev. B*, 1992, **46**, 6671–6687.

49 F. A. Lindemann, *Phys. Z.*, 1910, **11**, 609.

50 Y. Okamoto, F. Kawamura, Y. Ohta, A. J. Page, S. Irle and K. Morokuma, *J. Comput. Theor. Nanosci.*, 2011, **8**, 1755–1763.

51 A. J. Page, H. Yamane, Y. Ohta, S. Irle and K. Morokuma, *J. Am. Chem. Soc.*, 2010, **132**, 15699–15707.

52 Y. Shibuta and T. Suzuki, *J. Chem. Phys.*, 2008, **129**, 144102.

53 S. Chen, H. Ji, H. Chou, Q. Li, H. Li, J. W. Suk, R. Piner, L. Liao, W. Cai and R. S. Ruoff, *Adv. Mater.*, 2013, **25**, 2062–2065.

54 J. W. M. Frenken and J. F. V. D. Veen, *Phys. Rev. Lett.*, 1985, **54**, 134–137.

55 R. N. Barnett and U. Landman, *Phys. Rev. B*, 1991, **44**, 3226–3239.

56 Y. Zhou, M. Karplus, K. D. Ball and R. S. Berry, *J. Chem. Phys.*, 2002, **116**, 2323–2329.

57 V. H. Crespi, L. X. Benedict, M. L. Cohen and S. G. Louie, *Phys. Rev. B*, 1996, **53**, R13303–R13305.

58 H. Terrones, M. Terrones, E. Hernandez, N. Grobert, J. C. Charlier and P. M. Ajayan, *Phys. Rev. Lett.*, 2000, **84**, 1716.

59 S. Irle, G. Zheng, M. Elstner and K. Morokuma, *Nano Lett.*, 2003, **3**, 1657–1664.

60 A. J. Page, Y. Ohta, Y. Okamoto, S. Irle and K. Morokuma, *J. Phys. Chem. C*, 2009, **113**, 20198–20207.